Estimating Intensity Bias Fields in Confocal Images Showing Salient Cellular Arrangements

K. Mosaliganti[1], S. Singh[1], S. Naidu[2], J. Rittscher[3], R. Bhotika[3], R. Machiraju[1], K. Huang[4], G. Leone[2]

[1]Department of Computer Science and Engineering,
[2]Human Cancer and Genetics,
[3] Computer Vision Group, GE Global Research Center, Niskayuna, NY, USA
[4]Biomedical Informatics, The Ohio State University, Columbus, USA

***Abstract*— Spatial intensity inhomogeneities (bias fields) caused by effects such as signal attenuation and intensity saturation make the segmentation of confocal image data particularly challenging. In nuclei-stained images of tissue sections, cells often reside on surface manifolds (ducts, vasculature) and contribute yet another source of inhomogeneity due to inhomogeneous penetration of fluorescent dyes through the biological specimen. Here we propose a mathematical model for correcting the bias field that takes the location and local packing density of nuclei into account. The benefits of this bias estimation method are illustrated using data taken from mouse tumor micro-environment studies. Ground truth data, manually generated by domain experts, are used to compare the proposed bias estimation in combination with a state-of-the-art segmentation method.**

I. Introduction

In experimental studies such as those involving the tumor micro-environment, interactions between cellular constituents during signalling, normal development or disease pathology are important. Confocal laser scanning microscopy (CLSM) is an essential and widely used tool for the three-dimensional imaging method in these experiments. The 3*D* images with specific stains allows the delineation of cells and fine structures such as ducts, vasculature and tissue layers. The process of acquisition involves staining (or tagging) an entity-of-interest with histochemical and/or immunohistochemical markers that give a characteristic emission spectrum upon excitation by a laser source. However, spatial intensity inhomogeneities, also referred to as intensity bias fields, are observed in the collected 3*D* images.

A well-known manifestation of bias fields is observed as depth-dependent signal attenuation. Light transport through a specimen is fraught with photon absorption, refraction, scattering as well as spherical aberration effects [1]. Hence, photon intensities exponentially decrease as image planes are farther removed from the surface until a point is reached where the signal-noise ratio is abysmally low. The imaging depth is therefore limited by this phenomenon. Several techniques have been presented in literature that address axial intensity loss. These techniques propose multiplicative correction factors for each image plane based on either a filtering [2]–[4] or geometric approach [5], [6]. Can *et al.* [7] proposed a practical solution by imaging the sample from opposite views and fusing the resulting pair of data to improve the SNR of the reconstruction.

There are several other factors that cause bias fields such as image acquisition factors [8], variations of illumination exposure rate and spatially uneven distribution of dye [9]. Thus, it is very challenging to develop a correction method that is directly linked to the sources of heterogeneity. In this work, we correct inhomogeneity caused by the anisotropic packing density of cells in tissue matrices. Dense packing is observed near salient structures (ducts, vasculature) or in disease-states such as cancer. These regions affect dye-penetration leading to relatively high stain concentrations. During acquisition, the instrument point spread function (PSF) causes intensity saturation to occur in these regions leading to bias fields. Please refer to Figure 1(a), especially the area marked within the red circle. We observe that certain regions with high packing have relatively higher intensity values recorded. Furthermore, the contrast between nuclei and background is significantly diminished leading to poor signal-noise ratios (SNR).

Vovk *et al.* [10] review the extensive literature on inhomogeneity correction for MR datasets. Most methods are retrospective - completely based on the acquired image and some prior information about the imaged object. They are classified into four categories - filtering, surface-fitting, segmentation and histogram based. Of these, segmentation based correction strategies are the most prevalent owing to their dependence on image quality [11], [12]. Our approach can be categorized as a retrospective and segmentation based technique. However, we work with confocal microscopy datasets, utilize a nucleus intensity model and packing distributions and do not avail the use of anatomic atlases. In Section III, we compare our results with the *EMSegment* algorithm for MR image segmentation that available in the NAMIC *Slicer3* toolkit [12].

Here we propose an image formation model that models the bias field in confocal images depending on the presence of nuclei and their local packing density. The foreground maps and density estimates are integrated into a mathematical model of the imaging process which accounts for saturated regions and areas with poor contrast. Details are presented in section II. Nuclei foreground maps are estimated by correlating the image data with a template that models the intensity distribution for a nucleus which is stained with a fluorescent dye. 2-point correlation functions (2-*pcfs*) are used as efficient estimators of nuclei density [13]. These functions efficiently characterize

Corresponding author: Mosaliganti K., email: kishore@hms.harvard.edu

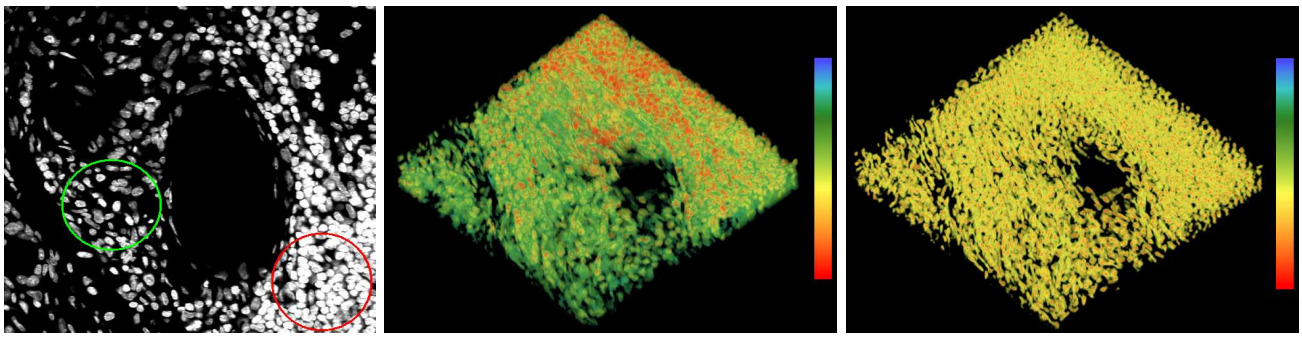

(a) (b) (c)

Fig. 1. (a) A confocal image plane drawn from a mouse mammary gland tissue section showing cellular arrangement near a duct. It is easy to see the saturation region and poor contrast in the dense regions. A 3D visualization of the raw dataset using a heat-map transfer function is shown (b) before and (c) after correcting for bias fields.

the microstructure phases in a heterogeneous substrate and have been applied to microscopy image segmentation [14]. The results, presented in section III, illustrate the performance of the method on real data. The discussion also includes a validation of the results.

II. Imaging Model

The key idea of our approach is the formulation of a mathematical model that describes how low contrast due to large support of the point spread function and saturation due to dye-penetration affect the image formation process. Let $\hat{I}(x)$ be the original intensity image that we wish to recover and the observed intensity image be $I(x)$. The image formation model is given as:

$$\begin{aligned} & I = \hat{I}e^{-\alpha F(x)(1-D(x))} + \beta D(x) \\ \Rightarrow \quad & \hat{I} = (I - \beta D(x))e^{\alpha F(x)(1-D(x))} \end{aligned} \tag{1}$$

where the functions F and D are continuous with range $[0,1]$. The function F is an indicator function for foreground voxels. The packing density of nuclei at the location x is modeled using the function D. This model integrates two key concepts: saturation in areas of high nuclei density and low contrast between nuclei and background in areas of low packing density. Parameters α and β are free parameters of the model and need to be learnt using training data.

a) **Saturation::** In regions of high nuclei density, saturation effects are observed in the image. Saturation in a region refers to the collective shifting of image intensities into higher ranges. Hence it can be modeled as an additive term depending on the nuclei density D. This is caused by the scattering of excitation and emitted light as well as the rapid variation in refractive indices locally. Regions of high saturation are observed to have higher intensities recorded.

b) **Low contrast::** Poor contrast between nuclei and background regions are caused by the large support of the point-spread function of the microscope. At background pixels, integration of light intensities from neighboring nuclei pixels leads to poor contrast regions.

The following sections explain how the foreground maps F and the packing density D can be estimated directly from the given image data. The estimation of the parameters α and β is based on the minimization of the coefficient of joint variation as outlined in Section III.

A. Nuclei Foreground Maps

Low contrast and saturation due to dye penetration pose make the segmentation of this data particularly challenging. Standard methods as for example thresholding (see Figure 4(a,b,c)), level-sets, or watershed algorithm typically do not lead to stable segmentations. Given the complexity of the given data sets that contain a large number of densely packed nuclei it is difficult to apply standard mixture-model based clustering approaches such as k-means or Expectation Maximization.

In order to make use of *a-priori* knowledge of the approximate shape, size and appearance of the nuclei we propose to correlate the data with a suitable template. This process leads to a probabilistic map, F for the foreground. Owing to the point-spread function (PSF) of the confocal microscope, they are imaged as diffuse objects in $3D$ with intensity maxima at the center. At the boundaries, intensity values gradually taper and merge with the background. In dense clusters, it is quite difficult to delineate boundaries of adjacent nuclei owing to partial voluming of signal intensities. Our core idea involves modeling intensity values of a salient nucleus with a Gaussian kernel centered at a mean pixel location and with a specific Σ. The proposed nucleus model is checked at each individual pixel in the observed image for correlation to yield a probabilistic map.

Distribution model: Let C_i represent a typical nucleus in the image I. Each cell may be attributed by its location ($p_i \in I$), its domain (or extent of support) (δ_i) and the corresponding intensity distribution $\mathscr{C}_i(x) : \delta_i(x) \rightarrow I$. Therefore, the nucleus C_i is represented by the triple $(p_i, \delta_i, \mathscr{C})$. Assuming that nucleus intensity values fit a Gaussian function of pixel locations, we write: $C_i = (a_i, N(p_i, \Sigma_i))$ where a_i is the peak intensity value. The following equations describe the reconstructed image $\hat{I}$ under our model.

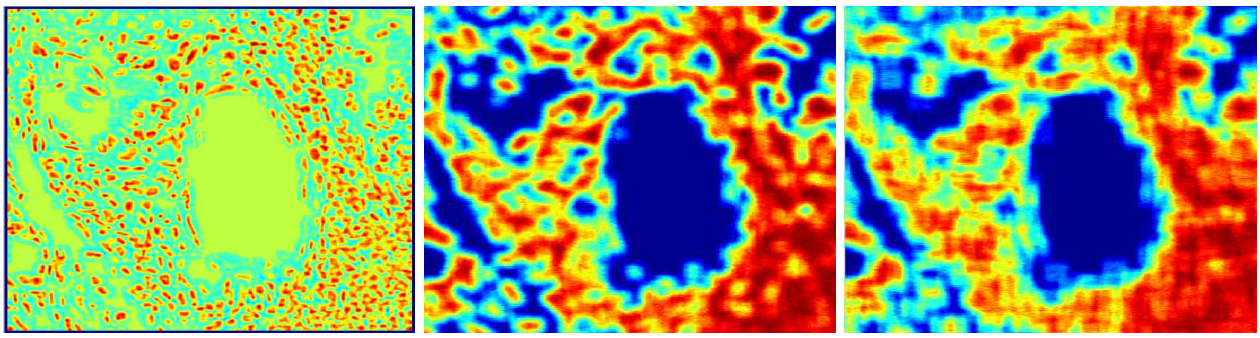

(a) (b) (c)

Fig. 2. (a) Nuclei foreground map F computed on the image in Figure 1(a). Each nuclei is assumed to have constant area with different anisotropic orientations. (b) The 2-*pcf* evaluated on the nuclei foreground with $k = 10$ pixel units and (c) $k = 15$ pixel units.

$$\mathscr{C}_i(x) = \frac{a_i}{2\pi^{\frac{3}{2}}|\Sigma_i|^{\frac{1}{2}}} \exp[-\tfrac{1}{2}(x-p_i)\Sigma^{-1}(x-p_i)^T] \quad (2)$$

$$\hat{I}(x) = \textstyle\sum_i \mathscr{C}_i(x) \quad (3)$$

Parameter Estimation: Ideally, we would like to automatically determine the parameters p_i and Σ_i for all nuclei in a given image I. We assume that nuclei have fairly constant volumes (say v) albeit with different eccentricities and orientations. Therefore, we impose the following constraint $|\Sigma_i| = \frac{3v}{4\pi}$ for each nucleus C_i. At any given pixel location p, we compute the correlation (ρ) of the image intensities with a normalized Gaussian kernel H with parameters (p, Σ). While p remains fixed during evaluation, the optimal Σ is determined by a gradient-descent optimization strategy. The correlation coefficient function $F(p)$ is determined in a neighborhood $\delta(p)$ such that 95% of the Gaussian template energy lies within. This arrangement ensures that neighboring nuclei, if present, do not influence the calculation of the correct Σ.

$$F(p) = \max_{\forall\Sigma} \rho(H(p,\Sigma),I)_{\delta(p)} \quad (4)$$

$$\Sigma_p = \arg\max_{\forall\Sigma} \rho(H(p,\Sigma),I)_{\delta(p)} \quad (5)$$

Figure 2(a) shows the foreground map $F(p)$ computed on the image plane earlier shown in Figure 1(a). It is easy to see that centers of nuclei have a high correlation values with the optimal Gaussian kernel. The correlation values tend to drop at boundaries since the intensity values do not locally fit a Gaussian distribution. Please note that $F(p) \in [-1,1]$ and is appropriately scaled when used as a probability mask in later sections. We now combine nuclei maps with the N-point correlation functions, that are described next, to estimate packing densities.

B. 2-Point Correlation Functions

One of the requirements in our imaging model was the selective identification of nuclei dense regions to enhance contrast and eliminate saturation. In this context, the 2-point correlation functions (2-*pcfs*) serve to estimate cellular packing densities and prevalent spatial distributions. We provide some background before explaining the use of these functions in our model. We recommend perusing [13] for full mathematical definitions, properties and references.

Let the background and nuclei foreground in the $3D$ image I be represented as phase 0 and 1 respectively. Consider placing a line segment with edge length k in I. The probability that both the vertices lie in phase 0 is defined as a 2-point correlation function (2-*pcf*), $D^k_{i_1 i_2}$, where $i_1 = i_2 = 0$. The subscripts denote the material phase at the vertices of the line segment in I. We now provide some insight into the probability measures captured by these functions. Consider the simple case of a 1-*pcf*, say D_0. It represents the probability that a point p is in phase 0. This quantity measures the volume fraction of phase 0 in the image. Similarly, D_1 is the volume fraction of phase 1 and we have $D_0 + D_1 = 1$. A 2-*pcf* is the probability of a straight line segment of length k randomly placed in I such that one end is in phase $i_1 \in \{0,1\}$ and the other end is in phase $i_2 \in \{0,1\}$. For an image containing two phases, there are four possible 2-*pcfs* namely D^k_{00}, D^k_{01}, D^k_{10} and D^k_{11}:

$$\begin{aligned} \sum_{i,j\in\{0,1\}} D^k_{ij} &= 1; \\ D^k_{01} &= D^k_{10}; \\ D^k_{00} + D^k_{01} &= f_0; \\ D^k_{10} + D^k_{11} &= f_1; \quad (6) \\ & \quad (7) \end{aligned}$$

Parameters f_0 and f_1 represent the volume fractions of the individual phases. Note that each salient region in an image with unique packing densities will provide a characteristic 2-pcf feature measure for a certain value of the separation distance k. The presentation of these characteristic values make regions to be easily identified. To estimate the 2-*pcf*, we resort to using Monte-Carlo sampling using a sliding window of dimensions Ω. To evaluate the 2-*pcf* at pixel location p, we place a number (S) of randomly oriented and positioned line segments of length k in its neighborhood. A large number of samples, $S = 500$ is chosen so as to increase the confidence in the computed result. k is chosen so that it denotes the average nuclei separation found in the images. Based on manual measurements, we determined $k = 15$ pixel units. Window neighborhoods with dimensions of $\Omega = [2k, 2k] = [30, 30]$ were

used. We then count the probabilistic fraction of line segments that have vertices (v_1,v_2) in phases (i,j) to give an estimate of the 2-*pcf* D^k_{ij}. Using Equation 4, the probabilities of a vertex v lying in the background (phase 0) and foreground (phase 1) is given by $F(v)$ and $\hat{F}(v) = (1-F(v))$ respectively. The function D^k_{11} allows us to selectively identify nuclei dense regions in conjunction with the foreground map F, both of which are used in the imaging model described in Section II.

$$\begin{aligned} D^k_{00}(p) &= \sum_{i=1}^{S} F(v_1)F(v_2); \\ D^k_{01}(p) &= \sum_{i=1}^{S} F(v_1)\hat{F}(v_2); \\ D^k_{11}(p) &= \sum_{i=1}^{S} \hat{F}(v_1)\hat{F}(v_2); \end{aligned} \tag{8}$$

III. Results

Our method was applied on 3*D* confocal datasets generated from a tumor micro-environment study in a mouse model. Each dataset was stained using Draq5 to highlight nuclei and had image dimensions of $512 \times 512 \times 100$. The dataset had a rich presence of cellular structures such as ducts and vasculature causing anisotropic packing densities to exist. In tumor regions, there was rapid proliferation of cells leading once again to dense regions. Earlier, in Figure 1, we showed 3*D* visualizations of a example raw and bias corrected dataset. Similar transfer functions were set in both cases to provide a qualitative evaluation of the performance. We observed that nuclei intensities did not suffer from spatial bias and had a good contrast with the background as indicated by the color map.

In order to evaluate the proposed bias correction technique we use it in conjunction with *EMSegment*, an EM segmentation algorithm that is part of NAMIC *Slicer3* toolkit [12]. *EMSegment* performs an optional bias segmentation step, which provides us with an opportunity to compare the optional build in bias estimation with our proposed method. As earlier explained in Section I, our method differs owing to the use of a generic nucleus intensity distribution model and a density estimator. To evaluate the performance of the three strategies, a pathologist reviewed eight (8) randomly selected sample images and manually segmented all the pertinent nuclei in each image. This served as the ground truth for our validation of the nuclei foreground. For the automatically segmented images, the following pixel counts were calculated (i) a - number of true positives (ii) b - false positives (iii) c - false negatives and (iv) d - true negatives. We use these counts to compute the *sensitivity*= $\frac{a}{a+c}$ and *specificity*= $\frac{d}{b+d}$ of the segmentation results. The results of this comparison are summarized in Figure 3. Note that (i) bias correction (triangle markers), in general, performs better than with no correction (circle marker) and (ii) our bias correction (inverted triangle) performs better than the custom-built bias correction (up triangle) in *EMSegment* quite significantly in terms of sensitivity while specificity values remain comparable. Upon closer analysis, the impact datasets (numbered 3-6) were found to be densely packed regions with saturation and showing low contrast thereby signifying the effectiveness of our strategy in those regions.

The inhomogeneity of the image can also been evaluated by measuring the intensity variation in the foreground and background. The coefficient of joint variation (*CJV*) was introduced in [15] as a method to compare bias-field correction methods for MRI datasets and has been extensively used for validation in MR literature [10]. *CJV* is defined as $CJV(C_1,C_2) = \frac{\sigma(C_1)+\sigma(C_2)}{|\mu(C_1)-\mu(C_2)|}$, where $\sigma(C)$ and $\mu(C)$ are the standard deviation and mean, respectively, of the object class C. We evaluated the *CJV* for 8 sets of segmented images. Figure 4 shows that the *CJV*'s for the corrected images are consistently better. Please note that we set parameters $\alpha = 0.8$ and $\beta = 0.05$ in our experiments. These values were chosen such that the *CJV* value with respect to the manually segmented images was minimized.

IV. Conclusion

The focus of this work is to correct spatial intensity inhomogeneities that exist in 3*D* confocal acquisitions due to anisotropic dye-penetration and saturation effects. The proposed mathematical model directly models the bias correction depending on the estimated nuclei foreground and the local nuclei packing density. Our results demonstrate that our model significantly improves the performance of state of the art segmentation methods. Manually segmented images were used as ground truth to calculate a quantitative comparisons of different methods.

References

[1] A. Diaspro, *Confocal and Two Photon Microscopy Foundations, Applications and Advances*, Willey-Liss, Inc., New York, 2002.

[2] P. Adiga and B. Chaudhuri, "Some efficient methods to correct confocal images for easy interpretation.," *Micron*, vol. 32, no. 4, pp. 363–370, 2001.

[3] A. Entwistle, "A method for the blind correction of the effects of attenuation and shading in light micrographs based upon moderated histogram equalization.," *Microscopy*, vol. 219, no. Pt 3, pp. 141–156, 2005.

[4] S. Lee and P. Bajcsy, "Intensity correction of fluorescent confocal laser scanning microscope images by mean-weight filtering," *Microscopy*, vol. 221, no. 2, pp. 122–136, 2006.

[5] C. Kervrann, D. Legland, and L. Pardini, "Robust incremental compensation of the light attenuation with depth in 3D fluorescence microscopy," *Microscopy*, vol. 214, no. 3, pp. 297–314, 2004.

[6] H. Wu and L. Ji, "Fully automated intensity compensation for confocal microscopic images," *Microscopy*, vol. 220, no. 1, pp. 9–19, 2005.

[7] A. Can, O. Al-Kofahi, S. Lasek, D. Szarowski, J. Turner, and B. Roysam, "Attenuation correction in confocal laser microscopes: a novel two-view approach," *Microscopy*, vol. 211, no. 1, pp. 67–79, 2003.

[8] J. Rigaut and J. Vassy, "High-resolution three-dimensional images from confocal scanning laser microscopy," *Anal. and Quant. Cytology and Histology*, vol. 13, no. 2, pp. 223–232, 1991.

[9] P. Oostveldt, F. Verhaegen, and K. Messens, "Heterogeneous photobleaching in confocal microscopy caused by differences in refractive index and excitation mode," *Cytometry*, vol. 132, no. 2, pp. 137–146, 1998.

[10] U. Vovk, F. Pernus, and B. Likar, "A review of methods for correction of intensity inhomogeneity in MRI," *IEEE Transactions on Medical Imaging*, vol. 26, no. 3, pp. 405–421, 2007.

[11] W. Wells, R. Kikinis, W. Grimson, and F. Jolesz, "Statistical intensity correction and segmentation of magnetic resonance image data," in *SPIE Proceedings of the Third Conference on Visualization in Biomedical Computing*, 1994.

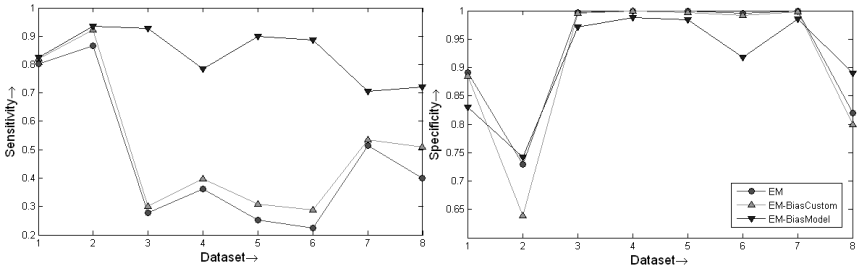

Fig. 3. **Plots of sensitivity and specificity using *EMSegment*.** We adopt three strategies for segmentation: (i) *EMSegment* with no bias correction involved (circle markers), (ii) *EMSegment* with in-built bias correction [12] (upright markers) and (iii) *EMSegment* with our bias correction (inverted markers). Note that we achieve the best results in terms of improved sensitivity and comparable specificities in all the 8 datasets.

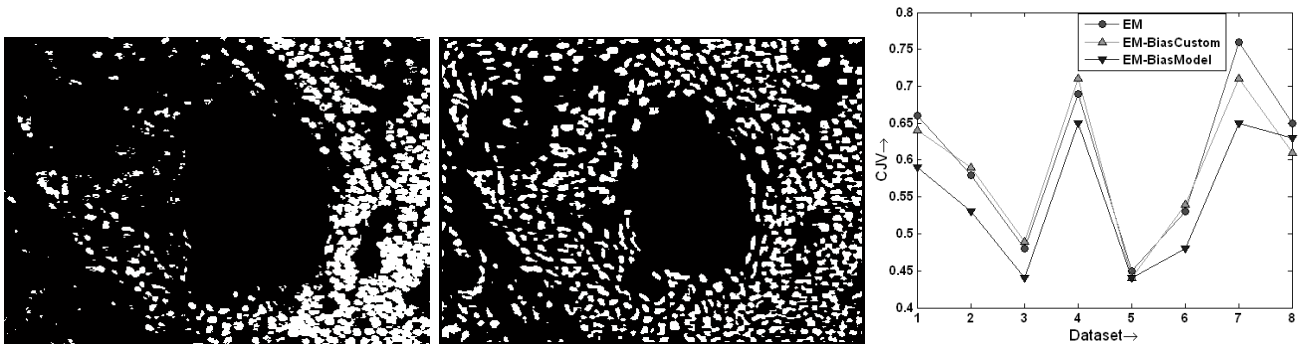

(a) (b) (c)

Fig. 4. **Comparing segmentations using CJV.** Here the coefficient of joint variation is used to compare the impact of the proposed bias correction method in combination with the *EMSegment* algorithm. (a) no bias correction. (b) *EMSegment* in combination with proposed bias correction method. (c) CJV given for the three segmentation approaches on eight different data sets. Note that the proposed bias estimation method significantly improves the segmentation results.

[12] K. Pohl, J. Fisher, J. Levitt, M. Shenton, R. Kikinis, W. Grimson, and W. Wells, "A unifying approach to registration, segmentation, and intensity correction," in *Medical Image Computing and Computer-Assisted Intervention*, 2005, vol. 3749, pp. 310–318.

[13] S. Torquato, *Random Heterogenous Material*, Springer Verlag, 2004.

[14] R. Ridgway, O. Irfanoglu, R. Machiraju, and K. Huang, "Image segmentation with tensor-based classification of N-point correlation functions," in *MICCAI Workshop on Medical Image Analysis with Applications in Biology*, 2006.

[15] B. Likar, M. Viergever, and F. Pernus, "Retrospective correction of MR intensity inhomogeneity by information minimization," *IEEE Trans. on Medical Imaging*, vol. 20, no. 12, pp. 1398–1410, 2001.